

Coherent manipulation of interacting electron qubits on solid neon

Xinhao Li,^{1,2, a)} Yizhong Huang,^{2,3} Xu Han,^{2,3} Xianjing Zhou,^{4,5, b)} and Dafei Jin^{6, c)}

¹⁾ *Department of Physics, Harvard University, Cambridge, Massachusetts 02138, USA*

²⁾ *Center for Nanoscale Materials, Argonne National Laboratory, Lemont, Illinois 60439, USA*

³⁾ *Pritzker School of Molecular Engineering, University of Chicago, Chicago, Illinois 60637, USA*

⁴⁾ *National High Magnetic Field Laboratory, Tallahassee, Florida 32310, USA*

⁵⁾ *Department of Mechanical Engineering, FAMU-FSU College of Engineering, Florida State University, Tallahassee, Florida 32310, USA*

⁶⁾ *Department of Physics and Astronomy, University of Notre Dame, Notre Dame, Indiana 46556, USA*

(Dated: 9 April 2025)

Solid neon has emerged as a pristine material host for electron qubits. Single electron-on-solid-neon (eNe) charge qubits have shown extraordinarily long coherence times and high operation fidelities. Realizing two-qubit gates in this platform is the next major step for realistic quantum information processing. In this work, we demonstrate frequency- and time-domain coherent manipulation of multiple eNe charge qubits that are coupled by charge interactions. Cross-resonance and bSWAP two-qubit gates are implemented, laying the foundation for universal quantum computing. An inter-qubit coupling strength exceeding 60 MHz has been observed, promising fast gate speed and suppressed infidelity. These results highlight the potential to scale up the eNe qubit platform toward universal quantum computing.

Electrons on solid neon (eNe) is an emerging solid-state qubit platform¹⁻⁴. Qubits based on charge states of eNe have shown great coherence performance and high-fidelity single-qubit operation because of the robust electron host environment offered by the neon layer². Meanwhile, the directness of charge qubits in terms of control and detection via electrical fields can largely simplify circuit design in a system with high qubit volume. To scale up charge qubits on solid neon, it is essential to demonstrate coherent interactions between them^{4,5}. In semiconductor electron hosts, strong coupling between qubits was initially established through charge interactions at short range⁶⁻⁸, which showcased the advantage of electron qubits in large-number integration on a small chip^{9,10}. For electrons on cryogenic substrates, charge interactions have also been proposed to perform two-qubit gates and establish entanglements^{4,11,12}.

Both theoretical and experimental results indicate the crucial role of the roughness of the neon surface in defining the properties of single qubits¹³⁻¹⁵, which could form during the current neon solidification process through its liquid phase. The surface profile could further provide the possibility for the local formation of multi-electron traps. Previously, we have observed the case of multiple electron qubits loaded onto a single niobium superconducting resonator². Even

though they simultaneously achieved strong coupling with the cavity, the inter-qubit coupling strength is small, preventing the demonstration of two-qubit operations. When two qubits are located close to each other, charge interaction strength could increase, surpassing the qubits' decoherence and enabling coherent two-qubit operation. Therefore, it is straightforward to pursue coherent local coupling between qubits on solid neon to demonstrate its scalability, which may also offer a unique testbed for studying the entanglement of electrons in free space and for the simulation of many-body quantum systems^{16,17}.

In this work, we achieve the coherent manipulation of multiple interacting electron qubits on solid neon in the circuit quantum electrodynamics architecture (cQED)^{18,19}. Qubit spectroscopy measurements show strong coupling between two qubits on solid neon with an inter-qubit coupling strength of $J/2\pi = 3.35$ MHz. Further, by driving one of the two qubits, which is strongly coupled with the superconducting resonator, we are able to demonstrate cross-resonance (CR) and bSWAP types of all-microwave two-qubit operations²⁰. The experiment results match well with theoretical simulations of the two-qubit coupled system based on characterized parameters. Moreover, we observe even stronger coupling within a three-qubit system, with a maximum coupling strength up to $J/2\pi = 62.5$ MHz. These results reveal the coherent interactions between qubits on solid neon, paving the way for further scaling up the system for applications in quantum computing and simulation.

Multi-qubit systems

We utilize the cQED architecture to drive and read out charge qubits on solid neon coupled with microwave photons within a superconducting resonator. Specifically, multiple qubits could exist on the neon film near the designed electron trapping area, as shown in Fig. 1a, whose coupling strength with the resonator is determined by the alignment between the qubits' dipole moments and the local microwave electrical field. For two closely arranged qubits Q_i and Q_j , they can directly couple with each other through charge interactions. The qubit-resonator system's Hamiltonian can be written as

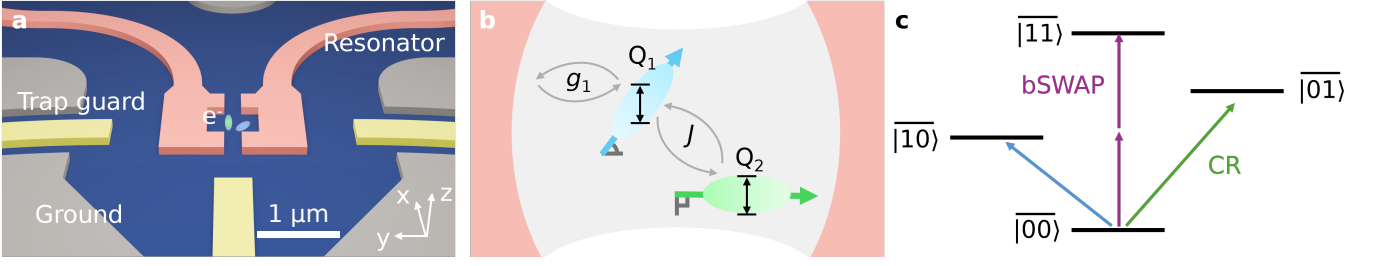


Fig. 1. Schematic of multi-qubit coupling on neon-covered superconducting resonator. **a**, Two closely arranged qubits trapped at the open end of a splitting co-planar waveguide superconducting resonator, surrounded by electrical gates-trap guards for tuning the qubits' transition frequency. **b**, Schematic of the interactions between qubits and the superconducting resonator, where Q_1 and Q_2 are coupled with strength J and Q_1 is coupled to the resonator with strength g . **c**, Energy level schematic of the two-qubit system showing possible transitions.

(refs. 21–23)

$$\begin{aligned}
 \hat{H}_{\text{sys}} &= \hat{H}_r + \hat{H}_q + \hat{H}_{\text{int}} \\
 \hat{H}_r &= \hbar\omega_r \hat{a}^\dagger \hat{a} \\
 \hat{H}_q &= \sum_i \frac{1}{2} \hbar\omega_i \hat{\sigma}_i^z \\
 \hat{H}_{\text{int}} &= \sum_i \hbar g_i (\hat{a}^\dagger \hat{\sigma}_i^- + \hat{a} \hat{\sigma}_i^+) \\
 &\quad + \sum_{ij} \hbar J_{ij} (\hat{\sigma}_i^+ \hat{\sigma}_j^- + \hat{\sigma}_i^- \hat{\sigma}_j^+)
 \end{aligned} \tag{1}$$

where \hat{H}_r , \hat{H}_q , and \hat{H}_{int} are the resonator, qubits, and interaction Hamiltonians. ω_r is the resonator frequency, ω_i is the transition frequency of Q_i , g_i is the coupling strength between the resonator and Q_i , J_{ij} is the inter-qubit coupling strength between Q_i and Q_j . \hat{a} and \hat{a}^\dagger are the annihilation and creation operators of resonator photons. $\hat{\sigma}_i^z$, $\hat{\sigma}_i^-$, and $\hat{\sigma}_i^+$ are the Pauli- z , lowering, and raising operators acting on Q_i . The system is driven by microwaves with a time-dependent amplitude $A(t)$ and frequency ω_d , and the driving Hamiltonian can be written as

$$\hat{H}_d = A(t) \cos(t\omega_d) \sum_i \hbar\eta_i (\hat{\sigma}_i^+ + \hat{\sigma}_i^-), \tag{2}$$

where η_i is the ratio for direct driving on Q_i (ref. 22). Because of the disordered neon surface, two closely arranged qubits may have distinct coupling strengths with the superconducting resonator, depending on their dipole orientation^{18,24}. As shown in Fig. 1b, inside a two-qubit coupled system, Q_2 with a dipole moment orthogonal to the MW field within a superconducting cavity could result in a close to zero qubit-cavity coupling strength. In such a case, if Q_1 is still coupled with the resonator via a finite dipole alignment, and Q_1 is interacting with Q_2 at a strength J , we will have a system Hamiltonian with $g_2 \sim 0$, $\eta_1 \sim 1$ and $\eta_2 \sim 0$ (ref. 22).

Such a two-qubit system could support all-microwave-driven two-qubit operations including the cross-resonance (CR) and bSWAP types of two-qubit gates,

as shown in Fig. 1c. For CR gates, Q_2 could be excited by driving Q_1 at the frequency of Q_2 , generating the transition $|00\rangle \rightarrow |01\rangle$ (refs. 21,25). For bSWAP gates, Q_1 and Q_2 could be driven monochromatically through a two-photon process near the frequency middle point between them, generating the transition $|00\rangle \rightarrow |11\rangle$ (refs. 22,26). All-microwave two-qubit gates are widely applied to fixed-frequency qubits thanks to their easy implementation, which also preserves the qubits' coherence by avoiding fast electrostatic and flux gating^{20,22,25,27,28}.

Two-qubit strong coupling

We have achieved a strong coupling between two qubits on solid neon. Figure 2a plots the two-tone measured qubit spectroscopy, in which we probe the system at the resonator frequency with low power, approximately -130 dBm reaching the resonator's input coupler, while sending a second continuous-wave tone with scanning frequency. Two clear avoided crossings are observed while tuning the bias voltage on the trap guard electrode (ΔV_{tg}), with a splitting magnitude of $J/2\pi = 3.35$ MHz, larger than the linewidth of the hybrid states above and below the splitting, as shown in Fig. 2b. This indicates the strong coupling between a qubit (Q_1), which is visible in the two-tone spectroscopy, and another invisible one (Q_2). Q_1 has a hyperbolic frequency dependency on ΔV_{tg} , with a charge sweet-spot (SS) located near 5.71 GHz, which is about 40 MHz above the resonator frequency at 5.668 GHz. The coupling between Q_1 and the resonator dispersively pushes the resonator spectrum, especially when Q_1 is tuned to its sweet-spot frequency, as shown in the Supplementary Information. Based on this, we estimate the coupling strength between Q_1 and the resonator to be $g_1/2\pi = 3.76$ MHz. In contrast, the interaction strength between Q_2 and the superconducting resonator is much weaker than that for Q_1 , resulting in negligible Q_2 -state-dependent resonator frequency shift and the invisible spectroscopy of Q_2 in Fig. 2a. In addition, the spectroscopic relations of the two splittings indicate that the frequency of Q_2 is much less sensitive to ΔV_{tg} compared to that for Q_1 , with a nearly constant frequency of 5.7261 GHz in the voltage scanning range of

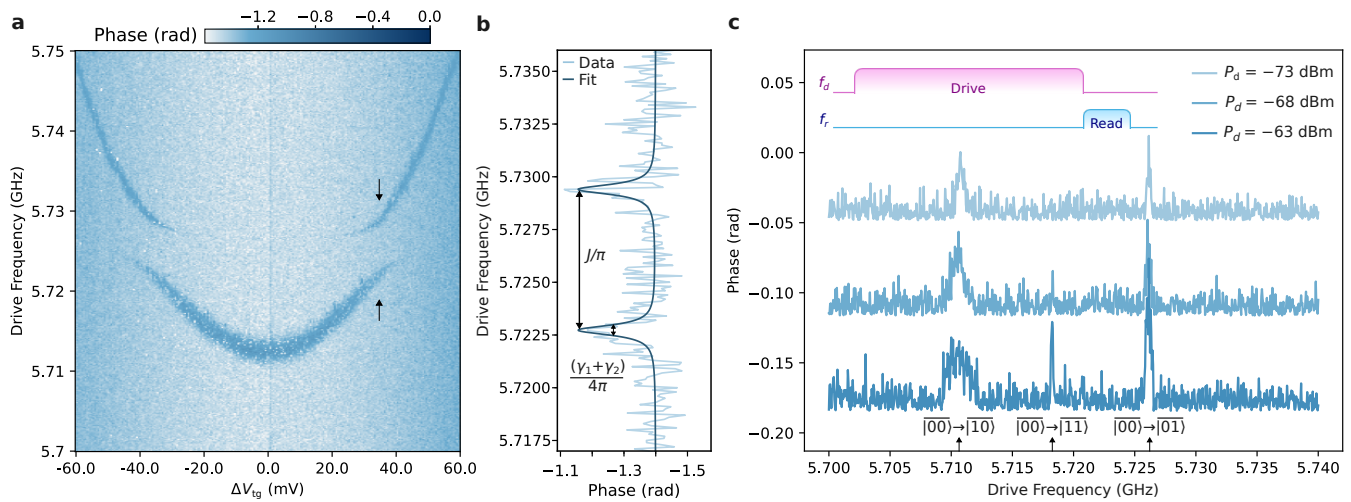


Fig. 2. Spectroscopic characterization of coherent two-qubit coupling on solid neon. **a**, Two-tone qubit spectroscopy with avoided splittings. **b**, Line cut of the two dressed states, at the black arrows in **a**, with splitting magnitude of $J/2\pi = 3.35$ MHz. **c**, Qubits spectroscopy measured with high-power pulsed readout. Driving pulse power reaching the resonator’s input coupler was increased from -73 dBm to -63 dBm, activating transitions corresponding to the CR and bSWAP two-qubit operations. The measurements were taken when system was biased at $\Delta V_{tg} = 0$ V. The phase curves are off-set for visualization.

Fig. 2a.

We attribute the two-qubit coupling to charge interactions at short range. The spectroscopic observations reveal a quantum system with two coherently coupled qubits on solid neon, while only one of them is strongly coupled to the superconducting resonator, corresponding to the system with $g_2 \sim 0$ and $\eta_2 \sim 0$. Due to the distinct coupling strengths between the two qubits and the resonator, we can rule out the case that the two qubits achieved strong coupling via virtual photon exchange through the resonator, in which the inter-qubit exchange strength $J = g_1 g_2 (1/\Delta_1 + 1/\Delta_2)/2$, where $\Delta_{1,2}$ are the detune between the qubits and the resonator²⁹.

Despite the fact that only Q_1 has a strong interaction with the superconducting resonator, we have managed to probe Q_2 utilizing the inter-qubit coupling. When biased at Q_1 ’s SS, instead of probing with continuous waves of weak power as in the case of Fig. 2a, we can first apply a long square pulse (10 μ s) with varying frequency followed by a short square probe pulse (700 ns) of high power (~ -100 dBm reaching the resonator) at the resonator frequency, shown as the inset pulse sequence in Fig. 2c. These parameters were chosen to balance the lifetime of Q_1 and the readout signal-to-noise ratio. The long driving pulse saturates the two-qubit system to a certain state. Following that, the high-power readout pulse will populate the resonator with average intra-cavity photon number \bar{n} and induce a blue ac-Stark shift of Q_1 at $2\bar{n}\chi$, due to the dispersive coupling between it and the resonator^{2,19}. Thanks to the undetectable coupling between Q_2 and the resonator, the probe signal will not affect Q_2 directly. Given the dispersive coupling strength of $\chi/2\pi \approx 0.33$ MHz, Q_1 ’s frequency can shift across Q_2 ’s

frequency as \bar{n} builds up and drops down, occurring at approximately $\bar{n} \sim 20$. Therefore, the pulsed probe will act as a SWAP operation between Q_1 and Q_2 (ref.²⁹), which eventually results in a Q_2 -state-dependent readout at the resonator frequency. This effect is turned-off when the probe tone is weak, as in Fig. 2a. See Supplementary Information for an example simulation of the SWAP due to the intra-cavity photon population.

As shown in Fig. 2c, with this method, we perform pulsed qubit spectroscopy when $\Delta V_{tg} = 0$ V. At low driving power, we observe two transitions at 5.711 GHz and 5.726 GHz, corresponding to frequencies of Q_1 at its SS and Q_2 . The appearance of $|00\rangle \rightarrow |01\rangle$ transition indicates that the long driving pulse excited Q_2 to a certain population, corresponding to the CR transition of a two-qubit coupled system^{21,25}, as shown in Fig. 1c. With an increase in the driving power, we observe another transition peak ($|00\rangle \rightarrow |11\rangle$) near the middle of the Q_1 and Q_2 frequencies at 5.718 GHz. This corresponds to the bSWAP type of two-qubit operation in Fig. 1c (refs.^{22,26}). In summary, through spectroscopic characterization, we have observed the coherent coupling between two qubits on solid neon, which can support both the CR and the bSWAP types of two-qubit operation.

Two-qubit gate operation

Following spectroscopic characterization of the coupled system, we perform pulse-driving two-qubit operations corresponding to the CR and bSWAP gates. Figure 3a plots the readout signal following Gaussian-shaped driving pulses with varying lengths and -70 dBm reaching the resonator input coupler. The pulses are truncated at $\pm 2.5\sigma$ on each side, where σ is the standard deviation

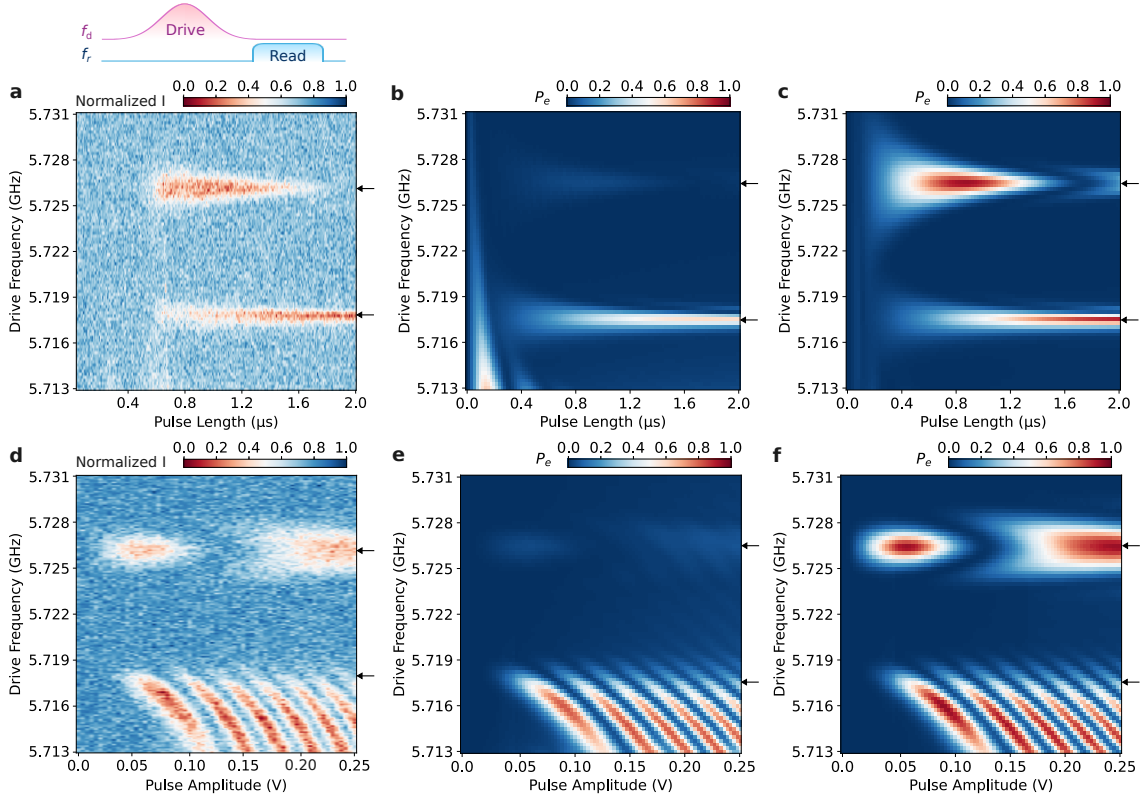


Fig. 3. Rabi oscillations of the two-qubit coupled system. **a**, Pulse length-frequency Rabi measurements showing the two operations corresponding to cross-resonance (CR) and bSWAP two-qubit gates. **b** and **c**, Simulation results of (b) Q_1 and (c) Q_2 excited state population evolution during pulse length-dependent Rabi measurement. **d**, Pulse amplitude-frequency Rabi measurements of the two-qubit operations. **e** and **f**, Simulation results of (e) Q_1 and (f) Q_2 population evolution during pulse amplitude-dependent Rabi measurement,

of the Gaussian envelope. The parameters of the readout pulses are the same as described in the last section. Two oscillation features corresponding to the CR operation near 5.726 GHz and the bSWAP operation near 5.718 GHz can be observed. Based on the system Hamiltonian, we numerically simulate qubit excited state population during the pulse-driving process³⁰. See Supplementary Information for simulation details. Fig. 3b and 3c plot the simulated excited state population evolution of Q_1 and Q_2 , matching the features of the two-qubit operations observed in experiments. The black solid lines in Fig. 4a and 4b plot the line cuts at these two oscillations, respectively. The blue and orange curves plot the simulated Q_1 and Q_2 excited state population after applying the driving pulse, matching the measured oscillation feature. For the CR operation, Q_2 was driven by driving Q_1 at the transition frequency of Q_2 , whose excited state population reached maximum when the pulse length was approximately 0.8 μs , as reflected in the readout in-phase signal (I). On the other hand, Q_1 was barely excited.

For the bSWAP operation, the two-photon process drives the two qubits simultaneously, while the oscillation frequency is much lower than the CR operation. Under a

square driving pulse with amplitude A , and negligible direct driving on the Q_2 , the oscillation frequency induced by CR operation is $\Omega_{|01\rangle} = AJ/(\Delta_{12} + 2J^2/\Delta_{12})$ (ref.²¹). In bSWAP operation, the oscillation frequency is approximately $\Omega_{|11\rangle} = 2A^2J/(\Delta_{12} + 2J^2/\Delta_{12})^2$ (ref.²²), where Δ_{12} is the frequency separation between Q_1 and Q_2 . When the bSWAP operation performs a π rotation, which is about 2 μs in our case, it is locally equivalent to an iSWAP gate with appropriate single-qubit rotations²².

In addition, we perform pulse amplitude-dependent Rabi oscillation measurement with a Gaussian-shaped driving pulse of 800 ns length and output pulse amplitude varying from 0.0 V to 0.25 V, corresponding to zero power to -57 dBm reaching the resonator input coupler. Again, we observe oscillating patterns near 5.726 GHz and 5.718 GHz, corresponding to the CR and bSWAP operations. We attribute the “waterfall-like” patterns in the frequency range between 5.713 - 5.718 GHz in Fig. 3d to the effects of the Gaussian pulse shape and the ac-Stark shift of Q_1 under higher driving power, which are reproduced by simulations in Fig. 3e and 3f. See detailed discussion in the Supplementary Information.

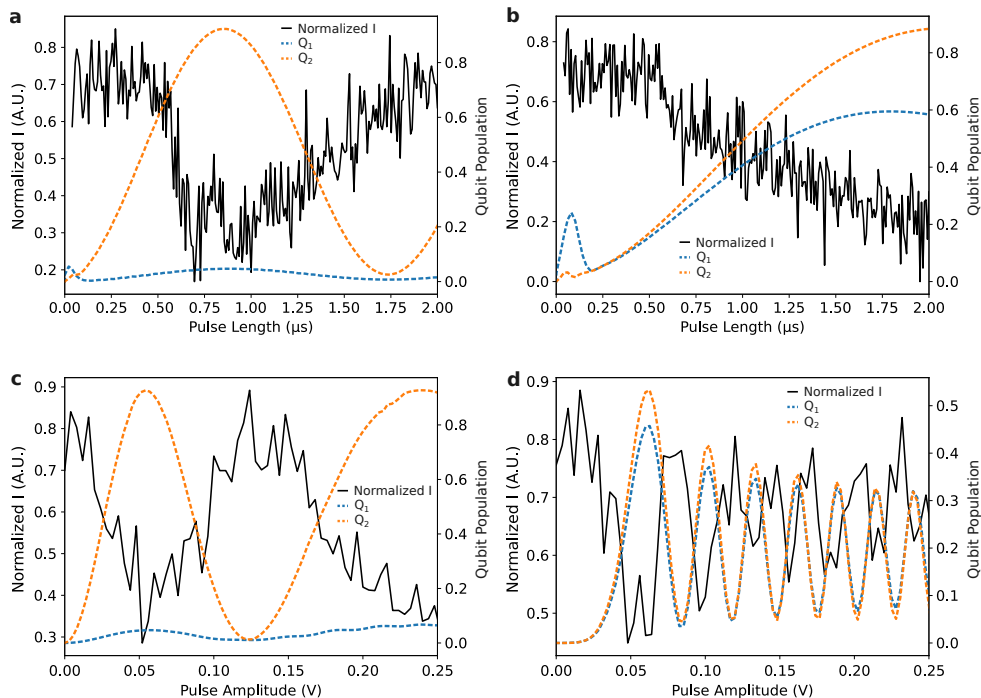


Fig. 4. All-microwave two-qubit operations on solid neon. **a** and **b**, Experiment recorded signal and numerical simulated qubits population evolution during pulse length-dependent Rabi measurements. Data are adopted from line cuts in Fig. 3a-c, corresponding to (a) CR and (b) bSWAP operations. **c** and **d**, Experiment recorded signal and numerical simulated qubit population evolution during pulse amplitude-dependent Rabi measurements. Data are adopted from line cuts in Fig. 3d-f, corresponding to (c) CR and (d) bSWAP operations.

In Fig. 4c and 4d, the line cuts at those two driving frequencies matched well with the numerically simulated qubit population evolution.

These results demonstrate, for the first time, two-qubit operations in a solid neon platform, revealing the potential for scaling up quantum systems based on charge qubits on solid neon. Further optimization of the two-qubit gate and readout is crucial to achieving high-fidelity operations.

Three-qubit strong coupling

To further demonstrate the scalability via charge interactions, we have managed to create a system with three qubits on solid neon. Figure 5a plots the two-tone measured qubit spectrum while varying the gate voltage on the resonator electrode (ΔV_{res}), revealing the energy diagram of this three-qubit system. One of them (Q_1) is directly coupled with a superconducting resonator, while the other two (Q_2 and Q_3) are serially coupled to Q_1 . Compared to Q_1 , the interactions strengths of Q_2 and Q_3 with the resonator are weak. We do not observe the avoided crossing between them and the resonator, and the dispersive phase shift of the resonator induced by Q_2 and Q_3 is also small when they are not hybridized with Q_1 .

In Fig. 5b, the line cut around $\Delta V_{\text{res}} = 0.74$ mV shows a coupling strength of $J_{12}/2\pi = 62.5$ MHz between Q_1

and Q_2 . On the other hand, the coupling strength $J_{23}/2\pi$ between Q_2 and Q_3 is much smaller, at approximately 5 MHz level. Due to the weak interaction between $Q_{2,3}$ and the resonator, we attribute the three-qubit coupling to charge interactions instead of virtual photon exchange via the resonator.

Figure 5c plots the calculated eigenstates of the system, which match well with the two-tone spectroscopy. Q_1 and Q_2 have closely arranged SS near 6.13 GHz, while Q_3 's SS is more detuned to approximately 5.91 GHz. All three qubits are responsive to the bias voltage on the resonator electrode with various sensitivity. See details in the Supplementary Information for those parameters applied in the calculation. Due to the strong coupling strength between Q_1 and Q_2 , the state mixing of the three qubits results in the energy diagram of the coupled system, which deviates from the undressed qubit spectrum. As a result, the three mixed states are all visible in the two-tone measurement in Fig. 5a. These observations indicate the possibilities of creating multi-qubit coupled systems on solid neon that can be applied for small- to middle-scale quantum simulations^{16,17}.

Discussion and outlook

In this work, we have realized coherently interacting multiple qubits on solid neon, mediated by charge interactions. In a two-qubit system, both spectroscopic

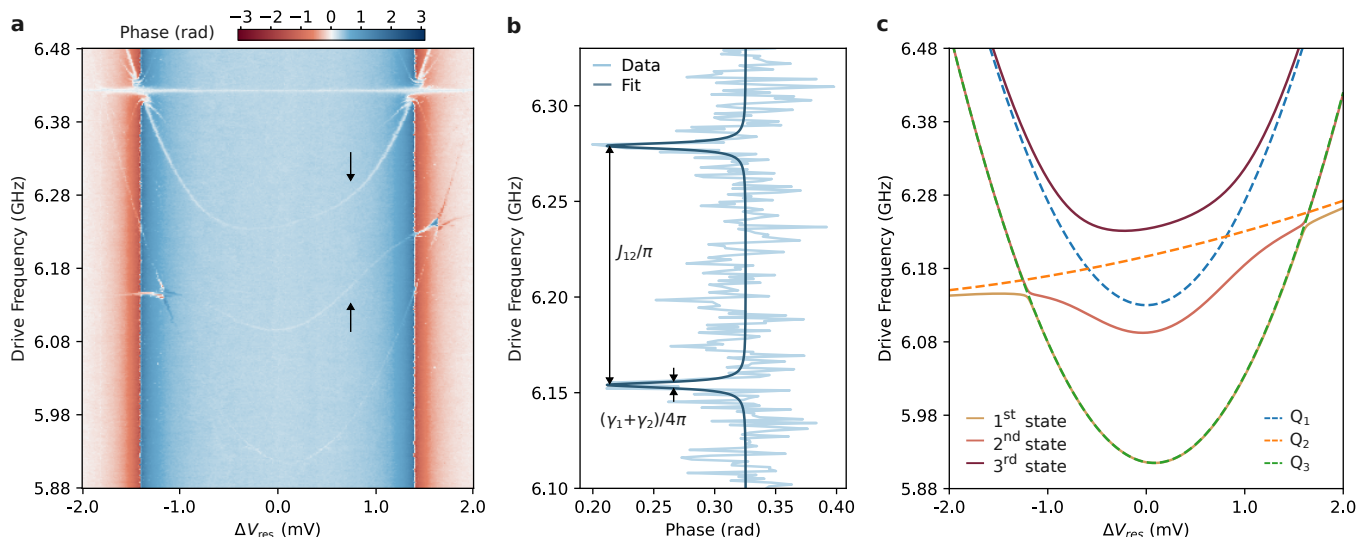


Fig. 5. Spectroscopic characterization of a three-qubit coupled system on solid neon. **a**, Two-tone measured qubits spectroscopy showing three-qubit coupled system **b**, The line cut showing large coupling strength between Q_1 and Q_2 of $J_{12}/2\pi = 62.5$ MHz. **c**, Calculated eigenstate energy diagram of the three-qubits coupled system, with undressed qubit states shown as dashed lines.

avoided crossing and time-domain pulse operation have demonstrated coherent qubit interactions. Cross-resonance and bSWAP two-qubit operation have been demonstrated, paving the way for the optimization of high-fidelity two-qubit gates on solid neon. Further, a three-qubit system with over 60 MHz inter-qubit coupling strength shows the potential of building more complex system with qubits on solid neon. In both of the two systems studied in this work, qubits can acquire distinct coupling strength with superconducting resonators. This offers the possibility to utilize qubits with dipole moment normal to the resonator microwave mode as quantum memories for other couples coupled to them^{31,32}, or as intermediate quantum buses³³. These observations also reveal the complexity of the charge environment on solid neon films and the potential effects of the neon surface profile in determining the qubit properties, including the interaction strength with resonators^{14,15}.

Establishing coherent interactions between qubits on solid neon is crucial for scaling up this emergent solid-state qubit platform. However, a multi-qubit system purely relying on charge interactions at short range will pose challenges to integrating control and read-out circuits. Entanglement between distant qubits through superconducting cavity buses could ease the limits on the local interaction^{29,34–36}. High-impedance resonators made of high-kinetic inductance thin films^{37,38} and Josephson junction arrays^{39,40} have been applied to achieve coherent interactions between distant semiconductor qubits. Further improvements in the control of individual qubit properties above solid neon and the development of a compatible frequency-tunable and high-impedance resonator would facilitate remote entanglement between distant qubits and hybridize it with

other quantum platforms^{32,41}. An on-chip quantum network will then be possible through the integration of interactions between qubits on solid neon at short and long ranges.

Methods

Devices and experiments

The data presented in Fig. 1 and 2 were collected on a high-impedance titanium nitride (TiN) splitting superconducting resonator, the same as the one in ref.¹⁴. The resonator supports a differential mode at 5.668 GHz with a total linewidth of $\kappa/2\pi = 0.38$ MHz. Electrodes with on-chip low-pass filters are connected to the resonator pins and trap guards surrounding the electron-trapping area to apply bias voltages for tuning qubits transition frequency. The device was mounted on a home-made printed circuit board (PCB), sealed in a copper cell with neon filling lines, tungsten filament, and electrical connectors on top of the cell lid. The cryogenic and room temperature electronics setups are the same as those in ref.¹⁴. The data presented in Fig. 3 were collected on a niobium splitting superconducting resonator, the same as the one in ref.^{1,2}. The resonator supports a differential mode at 6.426 GHz, with a total linewidth of $\kappa/2\pi = 0.46$ MHz. The sample mounting, cryogenic and room temperature electronic setups were the same as those in refs.^{1,2}.

The neon growth procedure is the same as that described in ref.¹⁴. In summary, the dilution fridge is warmed up to create a temperature gradient from ~ 27 K to ~ 25 K between its 4K plate and mixing chamber (MXC) plate. At that moment, neon gas is supplied from a room-temperature gas handling system in the form of

puffs and filled onto the device chip in the form of liquid. After a desired amount of neon filling, the fridge heater is turned off to let the fridge cool down to base temperature.

Electrons are deposited on to the chip by sending pulsed current on to the tungsten filaments mounted above the device chip. During the electron firing process, temperature sensed on the MXC plate can increase up to 100 mK. The details of the procedure and discussion of the electron deposition process can be found in ref. ¹⁴

Simulation of mutli-qubit coupled system

The populations of qubits in coupled systems are simulated based on their Hamiltonian, using the QuTiP package ³⁰. For the numerical data presented in Fig. 3, we use Eq. 1 and 2 as the Hamiltonian, with parameters listed in the Supplementary Information. The Lindblad master equation is applied to model the effects of relaxation and dephasing:

$$\begin{aligned} \frac{d\hat{\rho}}{dt} = & -\frac{i}{\hbar}[\hat{H}, \hat{\rho}] \\ & + \frac{\kappa}{2}(2\hat{a}\hat{\rho}\hat{a}^\dagger - \hat{a}^\dagger\hat{a}\hat{\rho} - \hat{\rho}\hat{a}^\dagger\hat{a}) \\ & + \sum_i \frac{\Gamma_i}{2}(2\hat{\sigma}_i^- \hat{\rho} \hat{\sigma}_i^+ - \hat{\sigma}_i^+ \hat{\sigma}_i^- \hat{\rho} - \hat{\rho} \hat{\sigma}_i^+ \hat{\sigma}_i^-) \\ & + \sum_i \frac{\Gamma_i^\Phi}{2}(2\hat{\sigma}_i^+ \hat{\sigma}_i^- \hat{\rho} \hat{\sigma}_i^+ \hat{\sigma}_i^- - (\hat{\sigma}_i^+ \hat{\sigma}_i^-)^2 \hat{\rho} - \hat{\rho} (\hat{\sigma}_i^+ \hat{\sigma}_i^-)^2) \end{aligned} \quad (3)$$

where $\hat{H} = \hat{H}_{\text{sys}} + \hat{H}_{\text{d}}$. $\hat{\rho}$ is the system density matrix. $1/\Gamma_i$ is the relaxation lifetime T_1 of Q_i , and $2/\Gamma_i^\Phi$ is the pure dephasing lifetime T_Φ of Q_i , which are adopted from relaxation and Ramsey measurements as shown in the Supplementary Information.

Data availability

The data that support the findings of this study are available from the corresponding authors upon request. Source data are provided with this paper.

Code availability

The codes used to perform the experiments and to analyze the data in this work are available from the corresponding authors upon request.

ACKNOWLEDGMENTS

D. J. and X. L. acknowledge support from the Air Force Office of Scientific Research (AFOSR) under Award No. FA9550-23-1-0636 for device fabrication and personnel effort. D. J., X. Z., and Y. H. acknowledge support from the Julian Schwinger Foundation for Physics Research for instrument development. D. J. acknowledges support from the Department of Energy (DOE) under Award No. DE-SC0025542 for solid-neon growth and characterization. D. J. acknowledges support from the National Science Foundation (NSF) under

Award No. OSI-2426768 for electron-on-solid-neon structural modeling. Work performed at the Center for Nanoscale Materials, a U.S. Department of Energy Office of Science User Facility, was supported by the U.S. DOE, Office of Basic Energy Sciences, under Contract No. DEAC02-06CH11357.

^aEmail: xinhaoli@fas.harvard.edu

^bEmail: xzhou4@fsu.edu

^cEmail: dfjin@nd.edu

- ¹X. Zhou, G. Koolstra, X. Zhang, G. Yang, X. Han, B. Dizdar, X. Li, R. Divan, W. Guo, K. W. Murch, *et al.*, “Single electrons on solid neon as a solid-state qubit platform,” *Nature* **605**, 46–50 (2022).
- ²X. Zhou, X. Li, Q. Chen, G. Koolstra, G. Yang, B. Dizdar, Y. Huang, C. S. Wang, X. Han, X. Zhang, *et al.*, “Electron charge qubit with 0.1 millisecond coherence time,” *Nature Physics* **20**, 116–122 (2024).
- ³W. Guo, D. Konstantinov, and D. Jin, “Quantum electronics on quantum liquids and solids,” *Progress in Quantum Electronics* **99**, 100552 (2024).
- ⁴A. Jennings, X. Zhou, I. Grytsenko, and E. Kawakami, “Quantum computing using floating electrons on cryogenic substrates: Potential and challenges,” *Applied Physics Letters* **124**, 120501 (2024).
- ⁵P. Platzman and M. Dykman, “Quantum computing with electrons floating on liquid helium,” *Science* **284**, 1967–1969 (1999).
- ⁶G. Burkard, T. D. Ladd, A. Pan, J. M. Nichol, and J. R. Petta, “Semiconductor spin qubits,” *Reviews of Modern Physics* **95**, 025003 (2023).
- ⁷J. R. Petta, A. C. Johnson, J. M. Taylor, E. A. Laird, A. Yacoby, M. D. Lukin, C. M. Marcus, M. P. Hanson, and A. C. Gossard, “Coherent manipulation of coupled electron spins in semiconductor quantum dots,” *Science* **309**, 2180–2184 (2005).
- ⁸F. Borsoi, N. W. Hendrickx, V. John, M. Meyer, S. Motz, F. Van Riggelen, A. Sammak, S. L. De Snoo, G. Scappucci, and M. Veldhorst, “Shared control of a 16 semiconductor quantum dot crossbar array,” *Nature Nanotechnology* **19**, 21–27 (2024).
- ⁹L. Vandersypen, H. Bluhm, J. Clarke, A. Dzurak, R. Ishihara, A. Morello, D. Reilly, L. Schreiber, and M. Veldhorst, “Interfacing spin qubits in quantum dots and donors—hot, dense, and coherent,” *npj Quantum Information* **3**, 34 (2017).
- ¹⁰A. Zwerver, T. Krähenmann, T. Watson, L. Lampert, H. C. George, R. Pillarisetty, S. Bojarski, P. Amin, S. Amitonov, J. Boter, *et al.*, “Qubits made by advanced semiconductor manufacturing,” *Nature Electronics* **5**, 184–190 (2022).
- ¹¹N. R. Beysengulov, Ø. S. Schøyen, S. D. Bilek, J. B. Flaten, O. Leinonen, M. Hjorth-Jensen, J. Pollanen, H. E. Kristiansen, Z. J. Stewart, J. D. Weidman, *et al.*, “Coulomb interaction-driven entanglement of electrons on helium,” *PRX Quantum* **5**, 030324 (2024).
- ¹²E. Kawakami, J. Chen, M. Benito, and D. Konstantinov, “Blueprint for quantum computing using electrons on helium,” *Physical Review Applied* **20**, 054022 (2023).
- ¹³T. Kanai, D. Jin, and W. Guo, “Single-electron qubits based on quantum ring states on solid neon surface,” *Physical Review Letters* **132**, 250603 (2024).
- ¹⁴X. Li, C. S. Wang, B. Dizdar, Y. Huang, Y. Wen, W. Guo, X. Zhang, X. Han, X. Zhou, and D. Jin, “Noise-resilient solid host for electron qubits above 100 mk,” *arXiv:2502.01005v2* (2025).
- ¹⁵K. Zheng, X. Song, and K. W. Murch, “Surface morphology assisted trapping of strongly coupled electron-on-neon charge states,” *arXiv preprint arXiv:2503.01847* (2025).
- ¹⁶T. Hensgens, T. Fujita, L. Janssen, X. Li, C. Van Diepen, C. Reichl, W. Wegscheider, S. Das Sarma, and L. M. Vandersypen, “Quantum simulation of a fermi–hubbard model using a semiconductor quantum dot array,” *Nature* **548**, 70–73 (2017).

- ¹⁷Y. Wang, Y. Chen, H. T. Bui, C. Wolf, M. Haze, C. Mier, J. Kim, D.-J. Choi, C. P. Lutz, Y. Bae, *et al.*, “An atomic-scale multi-qubit platform,” *Science* **382**, 87–92 (2023).
- ¹⁸D. Schuster, A. Fragner, M. Dykman, S. Lyon, and R. Schoelkopf, “Proposal for manipulating and detecting spin and orbital states of trapped electrons on helium using cavity quantum electrodynamics,” *Physical Review Letters* **105**, 040503 (2010).
- ¹⁹A. Blais, A. L. Grimsmo, S. M. Girvin, and A. Wallraff, “Circuit quantum electrodynamics,” *Reviews of Modern Physics* **93**, 025005 (2021).
- ²⁰P. Krantz, M. Kjaergaard, F. Yan, T. P. Orlando, S. Gustavsson, and W. D. Oliver, “A quantum engineer’s guide to superconducting qubits,” *Applied Physics Reviews* **6**, 021318 (2019).
- ²¹C. Rigetti and M. Devoret, “Fully microwave-tunable universal gates in superconducting qubits with linear couplings and fixed transition frequencies,” *Physical Review B* **81**, 134507 (2010).
- ²²S. Poletto, J. M. Gambetta, S. T. Merkel, J. A. Smolin, J. M. Chow, A. Córcoles, G. A. Keefe, M. B. Rothwell, J. Rozen, D. W. Abraham, *et al.*, “Entanglement of two superconducting qubits in a waveguide cavity via monochromatic two-photon excitation,” *Physical Review Letters* **109**, 240505 (2012).
- ²³E. Magesan and J. M. Gambetta, “Effective hamiltonian models of the cross-resonance gate,” *Physical Review A* **101**, 052308 (2020).
- ²⁴G. Koolstra, G. Yang, and D. I. Schuster, “Coupling a single electron on superfluid helium to a superconducting resonator,” *Nature communications* **10**, 5323 (2019).
- ²⁵J. M. Chow, A. D. Córcoles, J. M. Gambetta, C. Rigetti, B. R. Johnson, J. A. Smolin, J. R. Rozen, G. A. Keefe, M. B. Rothwell, M. B. Ketchen, *et al.*, “Simple all-microwave entangling gate for fixed-frequency superconducting qubits,” *Physical Review Letters* **107**, 080502 (2011).
- ²⁶M. Roth, M. Ganzhorn, N. Moll, S. Filipp, G. Salis, and S. Schmidt, “Analysis of a parametrically driven exchange-type gate and a two-photon excitation gate between superconducting qubits,” *Physical Review A* **96**, 062323 (2017).
- ²⁷J. M. Chow, J. M. Gambetta, A. D. Corcoles, S. T. Merkel, J. A. Smolin, C. Rigetti, S. Poletto, G. A. Keefe, M. B. Rothwell, J. R. Rozen, *et al.*, “Universal quantum gate set approaching fault-tolerant thresholds with superconducting qubits,” *Physical Review Letters* **109**, 060501 (2012).
- ²⁸A. D. Córcoles, J. M. Gambetta, J. M. Chow, J. A. Smolin, M. Ware, J. Strand, B. L. Plourde, and M. Steffen, “Process verification of two-qubit quantum gates by randomized benchmarking,” *Physical Review A* **87**, 030301 (2013).
- ²⁹J. Majer, J. Chow, J. Gambetta, J. Koch, B. Johnson, J. Schreier, L. Frunzio, D. Schuster, A. A. Houck, A. Wallraff, *et al.*, “Coupling superconducting qubits via a cavity bus,” *Nature* **449**, 443–447 (2007).
- ³⁰J. R. Johansson, P. D. Nation, and F. Nori, “Qutip: An open-source python framework for the dynamics of open quantum systems,” *Computer Physics Communications* **183**, 1760–1772 (2012).
- ³¹G. Wendin, “Quantum information processing with superconducting circuits: a review,” *Reports on Progress in Physics* **80**, 106001 (2017).
- ³²J.-k. Xie, R.-t. Cao, Y.-l. Ren, S.-l. Ma, R. Zhang, and F.-l. Li, “High-fidelity quantum memory with floating electrons coupled to superconducting circuits,” *Physical Review A* **110**, 052607 (2024).
- ³³T. A. Baart, T. Fujita, C. Reichl, W. Wegscheider, and L. M. K. Vandersypen, “Coherent spin-exchange via a quantum mediator,” *Nature Nanotechnology* **12**, 26–30 (2017).
- ³⁴J. Dijkema, X. Xue, P. Harvey-Collard, M. Rimbach-Russ, S. L. de Snoo, G. Zheng, A. Sammak, G. Scappucci, and L. M. Vandersypen, “Cavity-mediated iswap oscillations between distant spins,” *Nature Physics* **21**, 168–174 (2025).
- ³⁵L. Cheung, R. Haller, A. Kononov, C. Ciaccia, J. Ungerer, T. Kanne, J. Nygård, P. Winkel, T. Reisinger, I. Pop, *et al.*, “Photon-mediated long-range coupling of two andreev pair qubits,” *Nature Physics* **20**, 1793–1797 (2024).
- ³⁶C. Böttcher, S. Harvey, S. Fallahi, G. Gardner, M. Manfra, U. Vool, S. Bartlett, and A. Yacoby, “Parametric longitudinal coupling between a high-impedance superconducting resonator and a semiconductor quantum dot singlet-triplet spin qubit,” *Nature Communications* **13**, 4773 (2022).
- ³⁷P. Harvey-Collard, G. Zheng, J. Dijkema, N. Samkharadze, A. Sammak, G. Scappucci, and L. M. Vandersypen, “On-chip microwave filters for high-impedance resonators with gate-defined quantum dots,” *Physical Review Applied* **14**, 034025 (2020).
- ³⁸P. Harvey-Collard, J. Dijkema, G. Zheng, A. Sammak, G. Scappucci, and L. M. Vandersypen, “Coherent spin-spin coupling mediated by virtual microwave photons,” *Physical Review X* **12**, 021026 (2022).
- ³⁹A. Stockklauser, P. Scarlino, J. V. Koski, S. Gasparinetti, C. K. Andersen, C. Reichl, W. Wegscheider, T. Ihn, K. Ensslin, and A. Wallraff, “Strong coupling cavity qed with gate-defined double quantum dots enabled by a high impedance resonator,” *Physical Review X* **7**, 011030 (2017).
- ⁴⁰A. J. Landig, J. V. Koski, P. Scarlino, C. Müller, J. C. Abadillo-Uriel, B. Kratochwil, C. Reichl, W. Wegscheider, S. N. Coppersmith, M. Friesen, *et al.*, “Virtual-photon-mediated spin-qubit–transmon coupling,” *Nature communications* **10**, 5037 (2019).
- ⁴¹X.-F. Pan and P.-B. Li, “Nonlinear tripartite coupling of single electrons on solid neon with magnons in a hybrid quantum system,” *arXiv preprint arXiv:2503.08587* (2025).

Supplemental Information for Coherent manipulation of interacting electron qubits on solid neon

S1. RESONATOR DISPERSIVE SHIFT

Q_1 of the two-qubit coupled system presented in the main text is coupled to the resonator with its charge sweet-spot (SS) above the resonator frequency. Due to the interaction, the resonator is dispersively shifted when Q_1 is biased close to its SS, as shown in Fig. S1a. The line-cut of the resonator spectrum when ground-state Q_1 is on its SS shows $\chi/2\pi = 0.33$ MHz red shift compared to the bare resonator frequency, as shown in Fig. S1b. We estimated the coupling strength between Q_1 and resonator to be $g_1/2\pi \approx 3.76$ MHz based on this resonator dispersive shift and $\chi \approx g_1^2/\Delta_1$ (ref. ¹⁹), where $\Delta_1/2\pi = (\omega_1 - \omega_r)/2\pi \approx 43$ MHz.

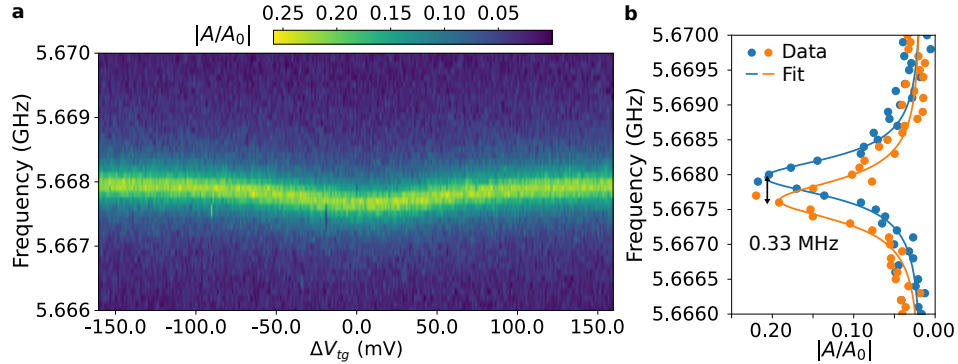


Fig. S1. Resonator dispersive shift caused by Q_1 . **a**, Resonator spectrum probe with varying bias on trap guard, showing the dispersive shift when Q_1 is close to resonator frequency. **b**, Transmission line cuts at bare resonator (blue dots and curve) and when Q_1 is biased at its sweet-spot (orange dots and curve).

S2. PULSED READOUT OF Q_2

We demonstrate the pulsed readout process of Q_2 with the following simulation. Initially, the population of Q_1 and Q_2 is set to be 0 and 1, respectively. Meanwhile, we assume the resonator is populated with the probe pulse, acquired photon-number of 1, 10 and 20. The free evolution of the coupled system is calculated with its Hamiltonian Eq. (1), and considering relaxation and dephasing with Eq. (4) of the main text. Figure S2 shows the evolution of Q_1 and Q_2 population under different photon population conditions. When the probe power is small, (Fig. 2a and 2b) the ac-Stark shift of Q_1 caused by the probe pulse is also small, Q_1 and Q_2 weakly exchange population at high

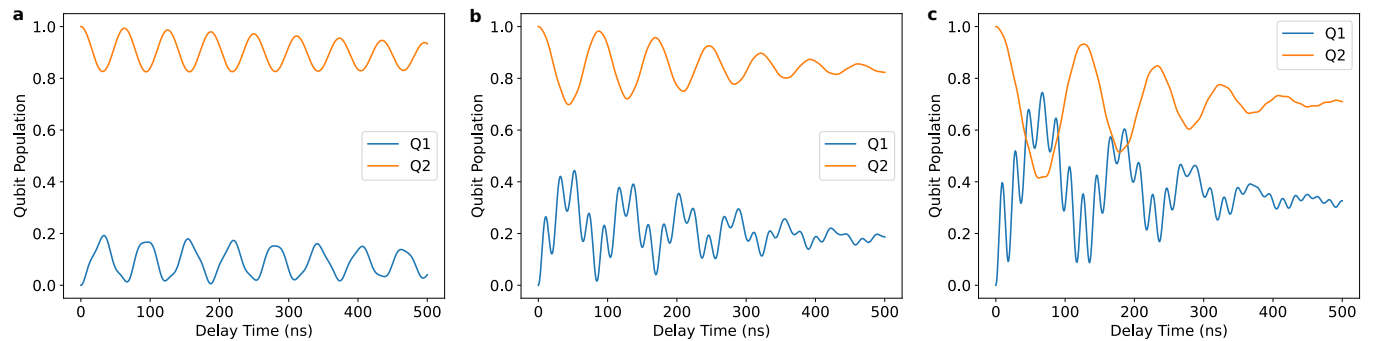


Fig. S2. Simulation of qubit population evolution with varying initial intra-cavity photon number. 500 ns free evolution simulated with initial photon numbers of (a) 1, (b) 10 and (c) 20, respectively. Blue curves show Q_1 population and orange curves show Q_2 population.

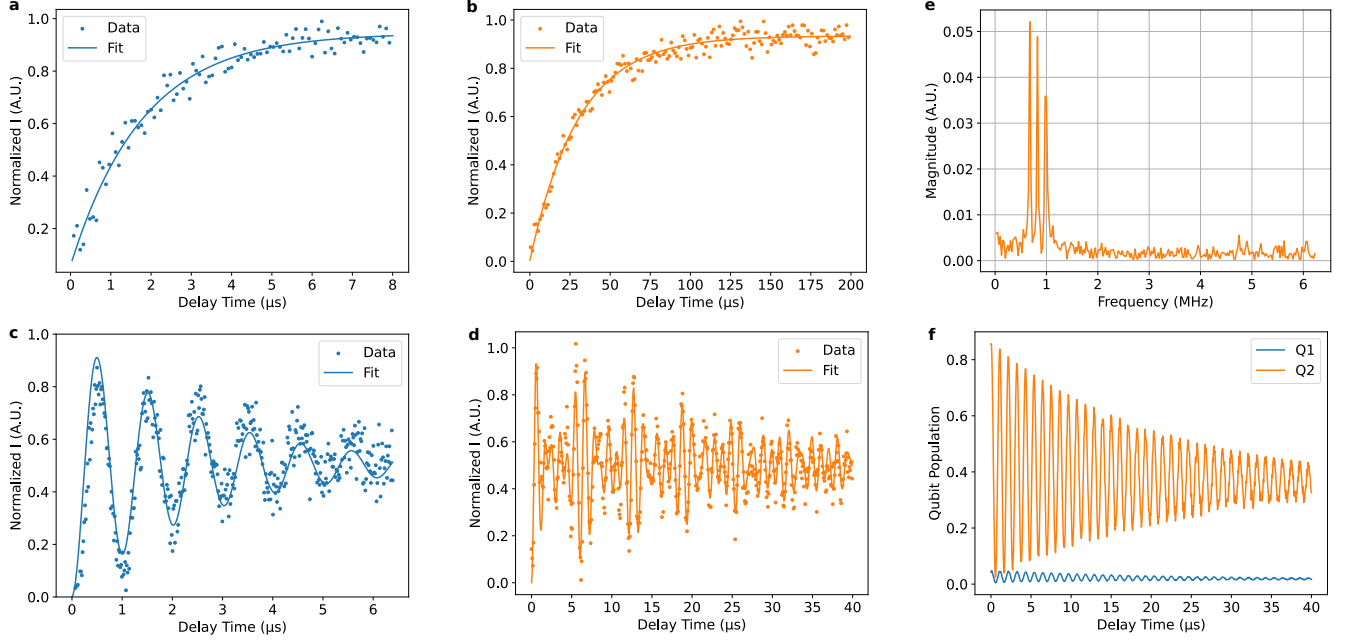


Fig. S3. Relaxation and decoherence of Q_1 and Q_2 . **a**, and **b**, Relaxation measurements of Q_1 and Q_2 with fitted T_1 of $1.8 \mu\text{s}$ and $30.3 \mu\text{s}$, respectively. **c**, and **d**, Ramsey measurements of Q_1 and Q_2 with fitted T_2^* of $2.56 \mu\text{s}$ and $32.99 \mu\text{s}$, respectively. **e**, Frequency components of the Ramsey fringes in **d**, revealing frequency fluctuations of Q_2 during the measurement. **f**, Numerical simulation of Ramsey measurement of Q_2 , indicating that the beating pattern in **c** is not intrinsically caused by the coupled system.

frequency approximately $\sqrt{\Delta_{12}^2 + 4J^2}$, where J is the inter-qubit coupling strength and Δ_{12} are the qubits detune. With increased photon number, the blue ac-Stark shift $2\chi\bar{n}$ causes the Q_1 across Q_2 frequency, resulting in their population swap at frequency close to $2J$, as shown in Fig. S2c. These simulation results reveal the readout process we applied to probe Q_2 , although its interaction strength with the resonator is small. The actual readout parameters are set to balance with the fast decaying of Q_1 , as illustrated in the following sections.

S3. QUBITS DECOHERENCE

We evaluated Q_1 and Q_2 's coherence via relaxation and Ramsey measurements when Q_1 was biased at its SS. Q_1 was directly driven by sending pumps through the resonator at its frequency. In contrast, Q_2 was driven by pumping Q_1 at Q_2 's frequency, corresponding to the cross-resonance (CR) two-qubit operation. Q_2 was probed with the pulsed readout method described in the main text and the previous section. Figure S3a and S3b show the relaxation of Q_1 and Q_2 with T_1 of $1.8 \mu\text{s}$ and $30.3 \mu\text{s}$, respectively, fitted from the measured in-phase signal. Figure S3c shows the Ramsey fringes of Q_1 , with a T_2^* of $2.56 \mu\text{s}$ fitted from the in-phase signal. The Ramsey measurement result of Q_2 is more complicated, as we observed multiple frequency components of the measured in-phase signal, as shown in Fig. S3d and S3e. Numerical simulation of the Ramsey measurement process with a stable single frequency of Q_2 reveals that the population swap between Q_1 and Q_2 induced by the inter-qubit coupling will not affect the final probed state and measured signal. Therefore, we attribute the beating features in Fig. S3d to fluctuations of the Q_2 's frequency during data acquisition, which occurred during other qubits measured on the same device, as in ref. ¹⁴. We fitted the data in Fig. S3d with a three-frequency model which resulted in a T_2^* of $32.99 \mu\text{s}$. The measured relaxation and decoherence rates are then used in the numerical simulation of the system.

S4. NUMERICAL SIMULATION PARAMETERS

Table SI summarizes the simulation parameters to build the Hamiltonian of the two-qubit coupled system and to account for the decoherence. In addition, the driving amplitude A in MHz used in the simulation is scaled with $A = 735 \times \mathcal{A}$, where \mathcal{A} is the experimental driving pulse amplitude in V.

	$\omega_i/2\pi$ (GHz)	$\kappa_i/2\pi$ (MHz)	$\gamma_i/2\pi$ (MHz)	$g_i/2\pi$ (MHz)	$J_{12}/2\pi$ (MHz)
Resonator	5.668	0.38	N.A.	N.A.	N.A.
Qubit 1	5.711	0.09	0.015	3.76	3.35
Qubit 2	5.726	0.005	0.027	0.0	

Tab. S1. Summary of the simulation parameters used for the two-qubit coupled system as in Fig. 3 and 4 of the main text.

To calculate the eigenstates of the three-qubit coupled system, as in the main text Fig. 4, we modeled qubits 1, 2, and 3 with hyperbolic frequency dependency on the gate voltage ΔV_{res} as: $f_i = \sqrt{(\alpha_i)^2 + (\beta_i \times (\Delta V_{\text{res}} - \delta_i))^2}$. Below, we list the parameters used to generate Fig. 4c in the main text. In addition, we used $J_{12}/2\pi = 62.5$ MHz and $J_{23}/2\pi = 5.0$ MHz.

	α_i (GHz)	β_i (GHz/mV)	δ_i (mV)
Qubit 1	6.130	1.325	0.0
Qubit 2	6.135	0.218	-4.0
Qubit 3	5.915	1.30	0.08

Tab. S2. Summary of the simulation parameters used for the three-qubit coupled system as in Fig. 5c of the main text.

S5. “WATERFALL” FEATURES IN PULSE AMPLITUDE-DEPENDENT RABI OSCILLATION

The “waterfall-like” pattern measured in pulse amplitude-dependent Rabi oscillation is also replicated in the numerical simulation, by realistically modeling the driving pulse with the same Gaussian envelope used in experiments. We attribute it to the combined effects of the pulse shape and ac-Stark shift of Q_1 under driving at the frequency middle point between Q_1 and Q_2 with high power. Figure S4 plots the simulation when we replace the Gaussian-shaped driving pulse with square pulses. Under such conditions, the “waterfall-like” pattern vanishes while we could still observe the red shift of the $|00\rangle \rightarrow |11\rangle$ transition at higher power, caused by the ac-Stark shift of Q_1 .

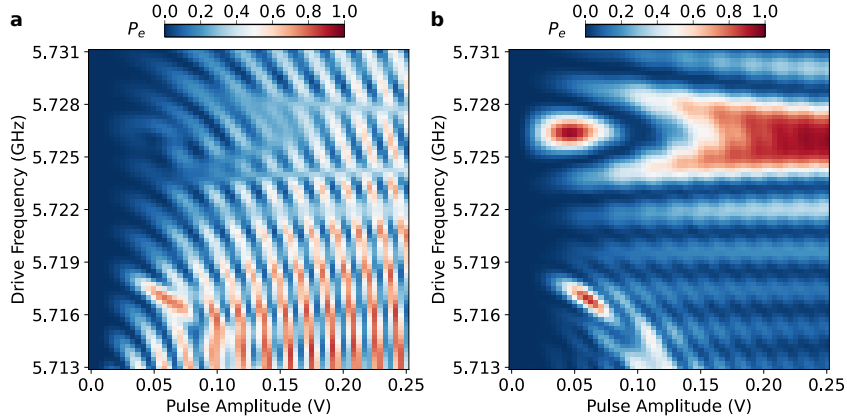


Fig. S4. Numerical simulation of pulse amplitude-dependent Rabi oscillation with step driving pulses. Simulation results of Q_1 (a.) and Q_2 (b.) population evolution, in which the “waterfall-like” pattern observed in experiments vanishes.